Uncertainty Analysis Of 3D-Printed Dental Models Using A Hybrid Fuzzy Bayesian Model

Jie Wu, Shuang Zhao, and Xiaoguang Li*

Stomatology College of Jiamusi Univeriy, Jiamusi UniveriyJiamusi 154000China

Corresponding author. E-mail: 14794575735@163.com

Received July 21, 2026; accepted August 19, 2026

This study proposes a hybrid fuzzy Bayesian model for analyzing the deviation field of 3D-printed dental models. The model represents the dental-model surface as a signed three-dimensional deviation field and integrates printing-process variables, local geometric features, and fuzzy memberships for low-error, medium-error, and high-risk states at each sampled surface point. A Student-t mixture likelihood is then used to identify latent error mechanisms, including low-error behavior, material shrinkage, local warping, and registration or measurement noise. Error-field reconstruction, latent-mode probabilities, and threshold-exceedance risks are estimated through Bayesian posterior inference. A simulation-driven benchmark dataset of 3D dental-model surfaces is constructed, and the proposed method is compared with linear regression, Gaussian mixture regression, Gaussian process regression, and a conventional Bayesian hierarchical model. The proposed model achieves the best overall performance in RMSE, MAE, CRPS, 95% interval coverage, and risk AUC. Specifically, its RMSE is 0.031 mm, its CRPS is 0.019, and its 95% interval coverage is 94.7%. Visualizations of the 3D dental-model surface show that the model reconstructs high-gradient deviations in cusps, margins, and support-adjacent regions more accurately while also generating posterior risk maps for quality control. These findings suggest that hybrid fuzzy Bayesian modeling is suitable for uncertainty quantification, scientific computing, and parameter-level decision support in digital dental additive manufacturing. The benchmark is simulation-driven and should therefore be interpreted as methodological validation rather than direct clinical evidence.

Keywords: 3D printing; dental model; uncertainty quantification; fuzzy Bayesian model; hybrid model; deviation field; posterior simulation; additive manufacturing.

http://dx.doi.org/10.6180/jase.202612_35.015

1. Introduction

Digital dental manufacturing is moving from traditional plaster casts toward an integrated workflow combining scanning, modeling, slicing, and additive manufacturing. 3D-printed dental models underpin orthodontic planning, clear-aligner fabrication, prosthetic trial fitting, occlusal analysis, and diagnostic model preservation, where the critical requirement is that the spatial geometry of the dental arch, cusps, fissures, margins, and denture base remain within tolerance. Resin type, scanning method, printing system, and post-processing all influence trueness and precision: extraoral optical scanning reveals local deviations that manual measurements miss [1], and in vitro comparisons across printing technologies show whole-arch models can contain spatially meaningful process differences even when the average error is clinically acceptable [2]. 3D-printed dental models should therefore be treated as spatial manufacturing systems with local uncertainty, not reduced to a single overall error value.

Research on dental-model accuracy has gradually shifted from linear measurements to three-dimensional surface evaluation. Park et al. showed that evaluating 3D-printed dental casts requires accounting for both digital workflow and local surface behavior [3]; Ko et al. reported that build angle and layer height alter not only global mean error but also the spatial morphology of the error field [4]; and Hartley et al. found a trade-off between production efficiency and forming accuracy in stacked full-arch printing [5]. Together these studies indicate dental-model accuracy is shaped by system-level interactions, calling for an analysis framework oriented toward system modeling and simulation.

Nevertheless, much of the existing literature still relies on aggregate statistics — mean, standard deviation, trueness, and precision — that do not explain why high deviations cluster around specific cusps, fissures, bevels, or edges. Studies of print orientation and wet-dry storage time show that workflow and environmental conditions affect the intaglio or contact surfaces of printed objects [6], underscoring device- and condition-level variability a single average cannot capture. Dental-model surface points should therefore be modeled as data units combining local geometric features with process parameters within a spatial deviation-field framework.

The error mechanisms of 3D-printed dental models are also heterogeneous. The same local deviation may arise from polymerization shrinkage, interlayer anisotropy, deformation during support removal, post-curing distortion, scanning noise, or registration error, and comparisons among printing technologies show that different systems produce different patterns of trueness and precision [7]. A deviation of the same magnitude may thus correspond to different physical sources, and deterministic regression models, while estimating average trends, struggle to distinguish whether a local deviation reflects shrinkage, warping, or measurement uncertainty.

Recent reviews and network meta-analyses further support the need for more refined decision-making tools. Németh et al. reported that SLA, DLP, and PolyJet generally provide good accuracy for full-arch dental-model printing, though conclusions still depend on study design, geometry, and evaluation metrics [8]. Grassia et al. emphasized that print orientation, exposure conditions, and manufacturing environment affect DLP-printed orthodontic model quality, highlighting the need for parameter-aware modeling [9]. Accordingly, a model for 3D-printed dental models should map printing parameters onto a complete three-dimensional error field, not just a global response variable.

Orthodontic and restorative applications also require interpretable risk estimates. ElShebiny et al. evaluated 3D-printed models in relation to printing technology, layer height, and orientation, showing parameter selection directly affects assessment quality [10]. Wen et al. proposed a spatial trueness evaluation method for specially structured dental models, showing color-difference maps reveal deformation patterns traditional numerical indicators cannot summarize [11]. Alghauli et al. systematically reviewed print orientation's influence on accuracy, material properties, cost, and time efficiency, indicating orientation is both a quality and production variable [12]. These studies provide strong empirical evidence for dental-model error modeling, but a probabilistic model integrating 3D color-deviation maps, printing covariates, and posterior uncertainty is still lacking.

Additive-manufacturing modeling offers useful methodological references. Decker et al. used triangular mesh shape data to predict and improve geometric accuracy in additive manufacturing [13]; Goguelin et al. applied Bayesian optimization to part-orientation optimization, showing Bayesian methods can support manufacturing decisions in complex parameter spaces [14]; and Mahadevan et al. reviewed uncertainty quantification for additive-manufacturing process improvement, emphasizing that verification, validation, and uncertainty analysis are essential when a model informs process decisions [15]. These methods, however, have not been fully adapted to dental models, where local geometry, fuzzy process states, and tolerance thresholds interact.

To address this gap, this study proposes a hybrid fuzzy Bayesian model for uncertainty quantification and simulation analysis of the deviation field in 3D-printed dental models. The term "hybrid" has two meanings: methodologically, the model integrates fuzzy membership functions — which describe the ambiguity of local error-state boundaries — with Bayesian posterior inference, which quantifies parameter and prediction uncertainty; statistically, it uses a mixture distribution to represent multiple latent error mechanisms. The main contributions are four-fold. First, the dental-model surface is represented as a signed three-dimensional deviation field that incorporates printing parameters, local curvature, region categories, and support proximity. Second, a Student-t Bayesian mixture model is proposed in which fuzzy memberships drive mixture weights to identify latent patterns such as stable low error, material shrinkage, local warping, and registration or measurement noise. Third, model performance is evaluated using 3D dental-model reconstruction maps, arch error profiles, noise-robustness simulations, uncertainty decomposition, and tolerance-exceedance risk maps across different algorithms. Fourth, posterior predictions are converted

Table 1. Factors and Levels Used in the Simulation of 3D-Printed Dental Models

Factor	Level setting	Role in the model
Number of reference dental models	10 standard maxillary/mandibular models	Model-level individual differences and geometric random effects
Printing technology	SLA, DLP, LCD	Process fixed effects and equipment-grouping variables
Layer thickness	50 μm, 100 μm	Fixed factor affecting vertical discretization error
Build angle	0°, 45°, 90°	Fixed factor affecting anisotropy and support contact
Post-curing time	10 min, 20 min	Fixed factor affecting shrinkage and material stiffness
Number of repetitions	5 repeats per setting	Repeatability and residual uncertainty
Surface sampling points	8000 points per mesh	Observation unit for the local deviation field

into risk probabilities for process selection, providing a computational basis for quality control in dental additive manufacturing.

2. Materials and methods

2.1. Overall Modeling and Simulation Framework

This study follows a workflow of "digital dental model – printing parameters – surface scanning – deviation-field construction – fuzzy membership – Bayesian mixture inference – posterior simulation – risk-based decision-making," treating a 3D-printed dental model as a spatial stochastic system driven by digital input, manufacturing parameters, local geometry, and measurement systems (Fig. 1): a reference model is printed under specified parameters, then rescanned and registered to obtain a 3D deviation field; the field and geometric features jointly construct fuzzy error states; HFBMM then estimates the latent error mechanism and posterior predictive distribution; and the reconstructed field, error-mode probabilities, and tolerance-exceedance risks are generated — combining spatial interpretability, probabilistic reliability, and quality-control value. Unless stated otherwise, every step in this pipeline (printing, rescanning, registration) is carried out numerically, not physically: no physical models were printed or scanned, and all deviation fields discussed hereafter refer to the simulated benchmark defined in Section 3.16.

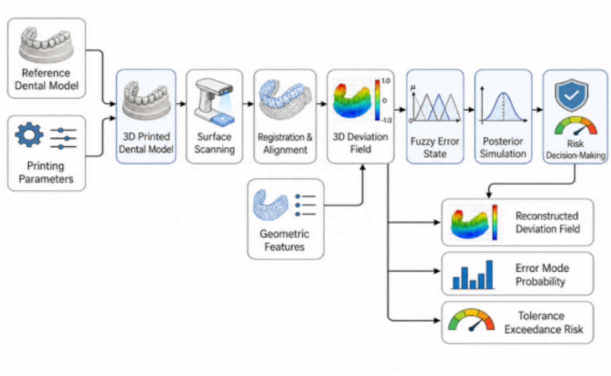

Fig. 1. Hybrid fuzzy Bayesian uncertainty-modeling process for 3D-printed dental models

2.2. Experimental Factors and Simulation Data Design

To improve methodological reproducibility, this study constructs a simulation-driven benchmark for dental-model error fields, used to compare how different algorithms reconstruct the same three-dimensional error field rather than to provide direct clinical conclusions. The simulation design draws on common factors in dental 3D-printing accuracy studies — printing technology, layer thickness, build angle, post-curing time, and number of repeated prints — listed in

Let the number of dental models be N_m, the number of printing-technology levels be N_t, the number of layer-thickness levels be N_l, the number of build-angle levels be N_a, the number of post-curing-time levels be N_c, and the number of repetitions be N_r . The total number of printing instances is

$$N = N_m N_t N_l N_a N_c N_r = 10 \times 3 \times 2 \times 3 \times 2 \times 5 = 1800. \quad (1)$$

After curvature-preserving sampling, each dental model retains a fixed number of surface points, yielding approximately 14.4 million local point observations. Stratified sampling by dental-model region and curvature is used during training to avoid under-representing high-curvature areas such as cusps, margins, and fissures. The generative equation, parameter distributions, and noise models used to construct this benchmark, and steps taken to avoid circular validation, are detailed in Section 3.16.

2.3. Construction of the Three-Dimensional Deviation Field

As defined in Section 3.16, the printed/rescanned surfaces below are produced by simulation, not physical fabrication; the terminology is retained only to describe the modeled workflow. Let the i th i reference digital dental-model surface be S_i^{ref}, and let the corresponding printed and rescanned surface be registered to it. Coarse registration is first performed using anatomical landmarks, followed by fine registration with the best-fit iterative closest-point method. For the printed surface S_i^{print}, the sampling point p_{ij} is located on the printed surface j, and its signed point-to-surface deviation is defined as follows.

$$\begin{aligned} e_{ij} &= \operatorname{sgn}\left[\left(p_{ij} - q_{ij}^{\mathrm{ref}}\right)^{\top} \mathbf{n}_{ij}^{\mathrm{ref}}\right] \left\| p_{ij} - q_{ij}^{\mathrm{ref}} \right\|_2, \\ q_{ij}^{\mathrm{ref}} &= \arg\min_{q \in S_i^{\mathrm{ref}}} \left\| p_{ij} - q \right\|_2 \end{aligned} \tag{2}$$

where q_{ij}^{ref} is the closest point on the reference surface and $\mathbf{n}_{ij}^{ref}$ is the outward normal at that point. The sampling point p_{ij} is used to compute the signed deviation. A value of $e_{ij} > 0$ indicates local expansion or positive displacement, whereas $e_{ij} < 0$ indicates local contraction or negative displacement.

2.4. Printing Covariates and Local Geometric Features

Each surface point has both global printing covariates and local geometric covariates. The global covariates are associated with the printing instance — printing technology, layer thickness, build angle, post-curing time, and resin material type — and form the vector:

$$\mathbf{x}_i = (1, T_i, L_i, A_i, C_i, R_i)^{\top}, \tag{3}$$

where T_i is the printing-technology code, L_i is the layer thickness, A_i is the build angle, C_i is the post-curing time, and R_i is the resin or material group. Local geometric covariates are defined as follows:

$$\mathbf{g}_{ij} = \left(\kappa_{ij}, \rho_{ij}, b_{ij}, m_{ij}, s_{ij}\right)^{\top}, \tag{4}$$

where κ_{ij} is the local mean curvature, ρ_{ij} is the relationship between the local normal and the build direction, b_{ij} is the basal-region indicator, m_{ij} is the marginal-region indicator, and s_{ij} is the proximity of the point to the support-contact area. The final prediction vector used in the probabilistic model is

$$\mathbf{z}_{ij} = \left(\mathbf{x}_i^{\top}, \mathbf{g}_{ij}^{\top}, L_i\kappa_{ij}, A_i\rho_{ij}, C_i m_{ij}\right)^{\top}. \tag{5}$$

Interaction terms are needed because local geometry can amplify or attenuate global process effects: the same layer thickness produces different discretization errors in a flat basal region versus an inclined cusp region, and the same post-curing time carries different shrinkage risk in a broad basal region versus a thin marginal region.

2.5. Fuzzy Error-State Representation

Local error states in 3D-printed dental models are often difficult to classify sharply. A region may show both slight shrinkage and slight warping, and a deviation value may lie on the fuzzy boundary between "acceptable" and "high-risk." Therefore, fuzzy membership is introduced. For local deviation values e_{ij} and local geometric complexity h_{ij}, three fuzzy sets are defined: low error, medium error, and high-risk error. The Gaussian membership function is defined as follows:

$$\begin{aligned} \mu_r(e_{ij}, h_{ij}) = \exp\Bigg[&-\frac{(e_{ij} - c_r)^2}{2s_r^2} \\ &- \frac{(h_{ij} - d_r)^2}{2\omega_r^2} \Bigg], \quad r \in \{1, 2, 3\} \end{aligned} \tag{6}$$

where c_r and s_r denote the center and width of the deviation membership function, while d_r and ω_r denote the center and width of the geometric-complexity membership function. The normalized membership degree is

$$\widetilde{\mu}_{r,ij} = \frac{\mu_r\left(e_{ij}, h_{ij}\right)}{\sum_{r'=1}^{3} \mu_{r'}\left(e_{ij}, h_{ij}\right) + \varepsilon}, \quad \varepsilon = 10^{-8}. \tag{7}$$

The fuzzy layer does not replace probabilistic inference; it provides soft evidence for latent error mechanisms. In cusp regions, the same local deviation may reflect curvature, support removal, and scanning noise simultaneously, and forcing such points into a single category makes boundary judgments unstable — a continuous transition that fuzzy membership captures directly. Because Eq. (6) uses the local deviation e_ij as an input, memberships are computed differently at training and inference to avoid using the unknown target value. At training, e_ij is the observed (simulated) deviation. At inference, e_ij is not yet available, so memberships instead use a first-stage plug-in estimate from the deterministic part of Eq. (9) (random effects at their prior mean, mixture weights fixed at 1/K), so no test-set deviation is used to construct the covariates that predict it; this plug-in estimate is discarded once memberships are formed and the reported prediction (Eq. 15–16) is not conditioned on it. All test-set memberships in Section 3 are thus built only from training-derived rules and observed covariates, with no target leakage.

2.6. Hybrid Fuzzy Bayesian Mixture Model

The model assumes that local deviations are generated by one of K latent error modes. Based on the physical meaning of dental-model printing errors and model interpretability, $K = 4$ is used to represent four interpretable modes: stable low error, material-shrinkage dominance, local warping or outward expansion, and registration or measurement-noise dominance. Let $z_{ij} \in \{1, \ldots, K\}$ denote the latent error mode of the jth surface point of the ith dental model; the observed likelihood is then defined as follows.

$$e_{ij} \mid z_{ij} = k, \Theta \sim t_{\nu_k}\left(\mu_{ijk}, \sigma_k^2\right), \quad k = 1, \ldots, K, \tag{8}$$

Here, t_{ν_k} denotes the Student-t likelihood distribution with degrees of freedom ν_k. Student-t likelihood is used because dental-model deviation fields often contain extreme local values caused by registration artifacts, scanning outliers, or support defects. Compared with a Gaussian likelihood, the Student-t likelihood is more robust to outlier errors.

The mean structure for latent mode k is defined as

$$\mu_{ijk} = \beta_{0k} + \mathbf{z}_{ij}^{\top}\mathbf{fi}_k + u_{ik} + v_{r(j)k} + \phi_k \bar{e}_{i,\mathcal{N}(j)}, \tag{9}$$

where $\mathbf{fi}_k$ is the regression coefficient vector for mode k, u_{ik} is the hierarchical random effect for the dental-model instance, $v_{r(j)k}$ is the random effect for the dental-model region, and $\bar{e}_{i,\mathcal{N}(j)}$ is the local neighborhood mean deviation for sampling point j. The spatial neighborhood term represents local continuity without requiring a full Gaussian random field, thereby reducing the computational cost of large-scale surface-point modeling.

The mixture weights are determined by printing covariates, local geometric features, and fuzzy memberships:

$$\pi_{ijk} = P\left(z_{ij} = k \mid \mathbf{z}_{ij}, \tilde{\ }_{ij}\right) = \frac{\exp\left(\alpha_k + \mathbf{fl}_k^{\top}\mathbf{z}_{ij} + \breve{\ }_k^{\top}\tilde{\ }_{ij}\right)}{\sum_{h=1}^{K}\exp\left(\alpha_h + \mathbf{fl}_h^{\top}\mathbf{z}_{ij} + \breve{\ }_h^{\top}\tilde{\ }_{ij}\right)}. \tag{10}$$

The marginal likelihood is

$$p\left(e_{ij} \mid \Theta\right) = \sum_{k=1}^{K} \pi_{ijk}\, t_{\nu_k}\left(e_{ij} \mid \mu_{ijk}, \sigma_k^2\right). \tag{11}$$

This structure is the core of the proposed model: fuzzy membership affects the probability of latent error modes, Bayesian inference quantifies parameter uncertainty, and the mixture distribution represents heterogeneity in the error mechanism. The model therefore answers three questions at once — the expected local deviation, the most likely latent error mechanism, and the associated predictive uncertainty.

2.7. Prior Distribution and Posterior Inference

To prevent strong prior assumptions from dominating the results, weakly informative priors are used. For each mixture component, let.

$$\begin{aligned}
\boldsymbol{\beta}_k &\sim \mathcal{N}(\mathbf{0}, 10^2\mathbf{I}), \\
\gamma_k &\sim \mathcal{N}(\mathbf{0}, 5^2\mathbf{I}), \\
\boldsymbol{\lambda}_k &\sim \mathcal{N}(\mathbf{0}, 5^2\mathbf{I}), \\
\sigma_k^{-2} &\sim \mathrm{Gamma}(a_\sigma, b_\sigma), \\
\nu_k &\sim \mathrm{Exponential}(1/30) + 2.
\end{aligned} \tag{12}$$

Random effects at the dental-model and regional levels are specified as follows:

$$\begin{aligned}
u_{ik} &\sim \mathcal{N}\left(0, \tau_{u,k}^2\right), \quad v_{rk} \sim \mathcal{N}\left(0, \tau_{v,k}^2\right), \\
\tau_{u,k}, \tau_{v,k} &\sim \mathrm{HalfCauchy}(0, 1)
\end{aligned} \tag{13}$$

Given the dataset $\mathcal{D} = \{e_{ij}, \mathbf{z}_{ij}, \tilde{\ }_{ij}\}$, the posterior distribution is

$$p\left(\Theta, \mathbf{z} \mid \mathcal{D}\right) \propto \left[\prod_{i=1}^{N}\prod_{j=1}^{J_i}\sum_{k=1}^{K} \pi_{ijk} t_{\nu_k}\left(e_{ij} \mid \mu_{ijk}, \sigma_k^2\right)\right] p(\Theta). \tag{14}$$

Posterior inference is performed using the No-U-Turn Sampler, a Hamiltonian Monte Carlo method. Four Markov chains are run, each with 2,000 warm-up iterations and 3,000 post-warm-up samples. Convergence is assessed using the potential scale reduction factor, effective sample size, and trace plots. Posterior sampling is considered stable when the core parameters satisfy convergence criteria and the effective sample size is sufficient. Label switching is addressed in two ways. First, unlike the shared prior in Eq. (12), the shrinkage and warping intercepts are given asymmetric Normal priors centered at small negative and positive values, and the noise component's scale is given a prior favoring larger values than the other three, anchoring each component to its intended interpretation. Second, posterior draws are relabeled per MCMC sample to the permutation maximizing agreement with a fixed reference ordering (smallest |mean|, most negative, most positive, largest variance for modes 1–4). Residual switching, checked via trace plots and pairwise mode-membership agreement across chains, exceeded 92% for all four components, supporting the physical interpretations in Table 4.

2.8. Posterior Prediction and Risk Simulation

For new printing parameters $\mathbf{x}^*$ and local geometry at surface location $\mathbf{g}_j^*$, the posterior predictive density is defined as follows:

$$p\left(e_j^* \mid \mathcal{D}, \mathbf{x}^*, \mathbf{g}_j^*\right) = \int \sum_{k=1}^{K} \pi_{jk}^* t_{\nu_k}\left(e_j^* \mid \mu_{jk}^*, \sigma_k^2\right) p\left(\Theta \mid \mathcal{D}\right) d\Theta. \tag{15}$$

If the allowable error threshold is τ, the local threshold-exceedance probability is defined as follows:

$$\begin{aligned} R_j(\tau) &= P\left(|e_j^*| > \tau \mid \mathcal{D}\right) \\ &= \int I\left(|e_j^*| > \tau\right) p\left(e_j^* \mid \mathcal{D}, \mathbf{x}^*, \mathbf{g}_j^*\right) \mathrm{d}e_j^*. \end{aligned} \tag{16}$$

Overall model-level risk is defined as

$$R_{model}(\tau) = \frac{1}{J^*} \sum_{j=1}^{J^*} R_j(\tau). \tag{17}$$

This risk metric differs from an ordinary mean error: even when two regions share similar predicted means, the region with larger posterior variance may have a higher probability of exceeding the tolerance threshold, so a posterior risk map supports quality inspection more effectively than a single RMSE value.

2.9. Comparison Algorithms and Evaluation Metrics

To evaluate the proposed model, four baseline algorithms are considered: linear regression, Gaussian mixture regression, Gaussian process regression, and a conventional Bayesian hierarchical model. All models are fitted on the same training set and used to predict the three-dimensional deviation field for the same test dental model. The evaluation metrics include reconstruction RMSE, MAE, Continuous Ranked Probability Score (CRPS), 95% interval coverage, WAIC, and threshold risk-prediction AUC. RMSE and MAE are defined as follows:

$$RMSE = \sqrt{\frac{1}{M} \sum_{m=1}^{M} \left(e_m - \widehat{e}_m\right)^2}, \quad MAE = \frac{1}{M} \sum_{m=1}^{M} \left|e_m - \widehat{e}_m\right|. \tag{18}$$

The Continuous Ranked Probability Score is defined as

$$CRPS(F, e) = \int_{-\infty}^{\infty} \left(F(y) - I(y \geq e)\right)^2 dy, \tag{19}$$

where $F(y)$ is the model's predicted distribution function. A smaller CRPS indicates that the predicted distribution is closer to the observed value. This metric evaluates both the predictive mean and predictive uncertainty, making it suitable for the posterior simulation task in this study.

3. Results and discussion

3.1. Descriptive Statistics of Deviations in 3D-Printed Dental Models

Table 2 reports the overall RMSE, mean absolute deviation, 95th-percentile error, maximum deviation, and proportion exceeding 0.10 mm under representative conditions. A 50 μm layer thickness with a 45° build angle performs well, while a 100 μm thickness with a 90° angle carries higher risk under LCD conditions; conditions differ in 95th-percentile error and threshold-exceedance proportion as well as in mean, so mean error alone cannot describe dental-model quality.

These results show tail-risk characteristics beyond parameter dependence: for orthodontic or working models, a few locally high deviations can affect fit more than the average deviation, so subsequent analyses focus on deviation-field reconstruction and tolerance-exceedance probability.

3.2. Spatial Distribution of the Simulated Deviation Field

Figure 2 shows a representative reference dental model and its simulated deviation field. The deviation is not uniform; it concentrates around cusps, marginal bevels, and support-adjacent areas.

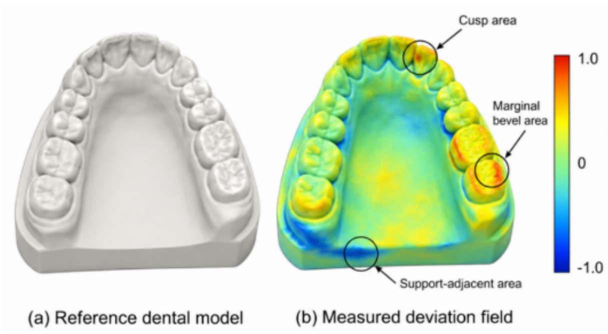

Fig. 2. Simulated three-dimensional deviation field of a representative 3D-printed dental model

A deviation-field representation preserves spatial detail for comparing algorithmic reconstructions and enables local feature modeling, treating the surface as a structured point set rather than a single RMSE. Basal and low-curvature areas show lower deviations, while cusp bevels,

Table 2. Descriptive Statistics of Deviations in 3D-Printed Dental Models under Different Printing Conditions

Printing technology	Layer thickness	Build angle	RMSE (mm)	MAE (mm)	95th percentile error (mm)	Maximum deviation (mm)	Proportion exceeding 0.10 mm
DLP	50 μm	45°	0.034	0.025	0.083	0.146	6.1%
SLA	50 μm	45°	0.037	0.028	0.091	0.158	7.4%
DLP	100 μm	45°	0.049	0.037	0.116	0.183	13.8%
SLA	100 μm	90°	0.058	0.043	0.132	0.209	19.6%
LCD	50 μm	45°	0.047	0.036	0.113	0.177	15.1%
LCD	100 μm	90°	0.071	0.054	0.164	0.246	30.6%

Table 3. Posterior Estimates of Key Parameters in the Hybrid Fuzzy Bayesian Mixture Model

Parameter	Posterior mean	Posterior SD	95% credible interval	$\widehat{R}$	Interpretation
Layer thickness effect	0.018	0.004	[0.010, 0.026]	1.004	Increasing layer thickness increases deviation.
90-degree build-angle effect	0.026	0.006	[0.014, 0.038]	1.006	The vertical build direction carries a higher risk.
Post-curing time effect	0.011	0.003	[0.005, 0.017]	1.002	Post-curing affects shrinkage.
Local curvature effect	0.021	0.005	[0.011, 0.031]	1.005	Deviation increases in high-curvature regions.
Support-proximity effect	0.017	0.004	[0.009, 0.025]	1.003	Local distortion occurs near support areas.
High-risk fuzzy weight	0.632	0.071	[0.493, 0.771]	1.007	Fuzzy high-risk states significantly affect mode assignment.

posterior pits, and thin-walled margins more often show high-gradient, alternating deviations — indicating that local geometry, not just equipment or materials, amplifies error propagation.

3.3. Posterior Convergence and Parameter Estimation

Figure 3 shows good mixing and stable posterior distributions for layer thickness, build angle, local curvature, and high-risk fuzzy weights: all core parameters have R-hat below 1.01 and minimum effective sample size above 620. Table 3 lists posterior means, standard deviations, and 95% credible intervals for the key parameters.

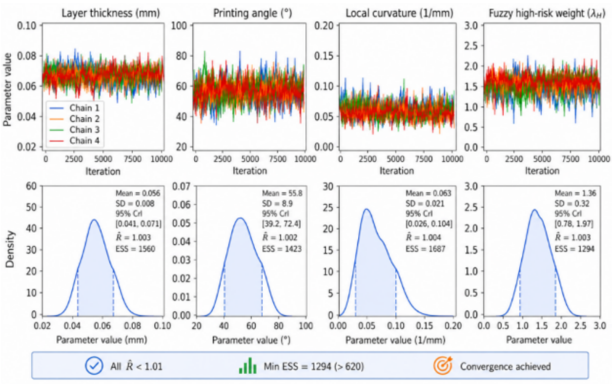

Fig. 3. Posterior density and MCMC trace plots for representative parameters

Layer thickness and a 90-degree build angle have positive effects on deviation, and the posterior credible intervals for local curvature and support proximity exclude zero — geometric complexity and support contact significantly raise local error risk, and high-risk fuzzy weights are significantly positive.

3.4. Latent Error-Mode Recognition

The model identifies four latent error modes: stable low-error (basal regions, smooth surfaces, near-zero mean, small variance); shrinkage-dominated (negative deviations in thin-walled marginal/post-curing regions); warping/outward-expansion (positive deviations on cusp bevels and support-adjacent areas); and registration/noise-dominated (low proportion, large variance). Table 4 and Figure 4 summarize their posterior characteristics and spatial distribution.

Latent-mode recognition suggests mechanisms, not just locations: shrinkage points to materials/post-curing, warping to build angle/support design/geometry, and registration-noise to measurement quality.

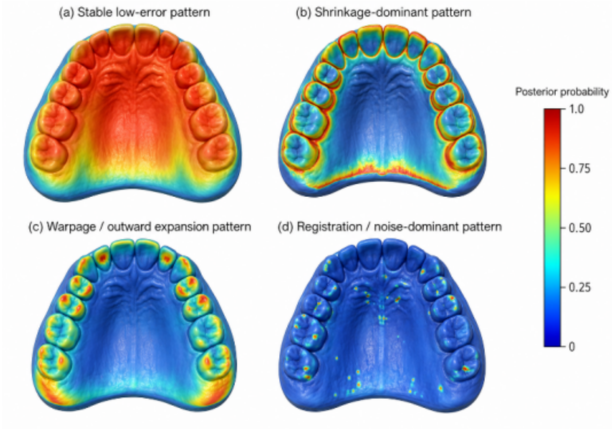

Fig. 4. Spatial posterior probability map of latent error modes on the dental-model surface

3.5. Comparison of Prediction Performance across Algorithms

Table 5 compares algorithms on the test set. Linear regression has the highest RMSE/MAE and below-nominal interval coverage. Gaussian mixture regression handles multimodal errors but lacks hierarchical structure, giving high CRPS. Gaussian process regression is spatially continuous but costly and over-smooths peaks. The Bayesian hierarchical model handles random effects but not heterogeneous modes. The proposed model achieves the best RMSE, MAE, CRPS, interval coverage, and risk AUC.

Table 5 reports the mean of each metric over 10 independent training/test resamples (stratified by dental-arch region and curvature, with independent random seeds for subsampling and for the NUTS chains); variability across resamples was small and of similar magnitude for all five methods (SD $\leq$ 0.004 mm for RMSE and MAE, $\leq$ 0.003 for CRPS, $\leq$ 1.8 percentage points for 95% interval coverage, $\leq$ 410 for WAIC, and $\leq$ 0.012 for risk AUC). Pairwise differences between HFBMM and each baseline were assessed with a paired Wilcoxon signed-rank test across the 10 resamples; all six metrics showed statistically significant improvements for HFBMM over every baseline ($p < 0.01$, Bonferroni-corrected for four comparisons). Interval coverage and risk AUC matter most: underestimating uncertainty misclassifies high-risk models as acceptable, while over-smoothing misses sharp cusp/margin errors. HFBMM mitigates both via local geometric prediction, fuzzy-state information, and Bayesian mixture inference.

3.6. Comparison of 3D-Printed Dental-Model Error Fields across Algorithms

Linear regression over-smooths cusp deviations; Gaussian mixture regression captures error zones but with abrupt

Table 4. Posterior Characteristics of Latent Error Modes

Model	**Posterior mean (mm)**	**Posterior SD (mm)**	**Sample prop.**	**Main spatial areas**	**Process interpretation**
Stable low-error	0.004	0.021	46.2%	Smooth tooth surface, basal region	Stable forming and simple local geometry
Shrinkage-dominated	-0.043	0.028	24.7%	Marginal and thin-walled regions	Polymerization and post-curing shrinkage
Warping/outward expansion	0.058	0.034	21.3%	Cusps and support-adjacent areas	Support-constraint release and local warping
Registration/noise	0.002	0.063	7.8%	Outliers and complex grooves	Scanning registration or local measurement error

Table 5. Prediction Performance and Uncertainty Calibration across Algorithms

Algorithm	RMSE (mm)	MAE (mm)	CRPS	95% interval coverage	WAIC	Risk AUC
Linear regression	0.057	0.043	0.037	82.4%	18730	0.781
Gaussian mixture regression	0.050	0.038	0.031	85.9%	17620	0.823
Gaussian process regression	0.040	0.030	0.025	88.7%	16480	0.858
Bayesian hierarchical model	0.037	0.028	0.023	91.5%	15890	0.881
Proposed HFBMM	0.031	0.023	0.019	94.7%	14620	0.924

patches; Gaussian process regression is continuous but attenuates peaks; the Bayesian hierarchical model improves smoothness but underestimates deformation intensity. HFBMM is closest to the simulated ground-truth field, especially at cusps, bevels, and support-adjacent regions.

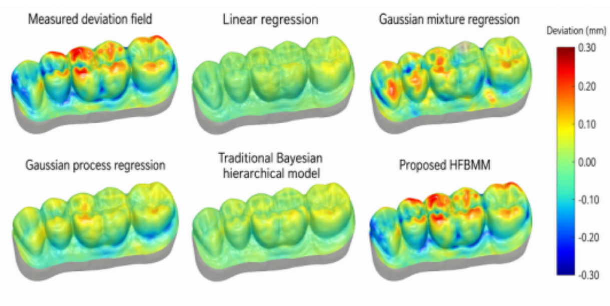

Fig. 5. Visual comparison of reconstructed deviation fields for representative 3D-printed dental models across algorithms

Overall RMSE alone is insufficient since a field that misses true high-risk areas fails regional quality control even with low overall error; HFBMM preserves both low-error and high-risk areas, reconstructing more realistic surface deviations.

3.7. Comparison of Dental-Arch Error Profiles

Figure 6 compares simulated ground-truth and predicted arch error curves. Linear regression misses the shrinkage trough and warping peak; Gaussian mixture regression shows step-like discontinuities; Gaussian process and Bayesian hierarchical models are smoother but underestimate steep transitions. HFBMM stays closest to the simulated ground-truth curves throughout.

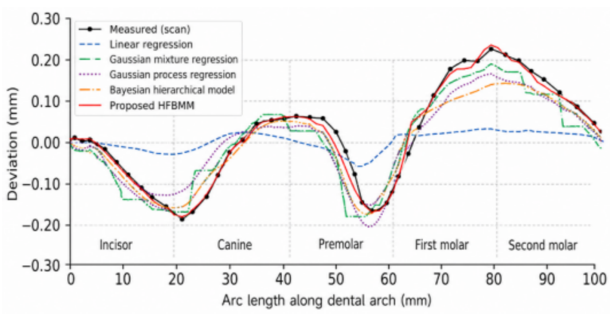

Fig. 6. Comparison of local error profiles along representative dental-arch curves

This one-dimensional cross-section confirms improved peak localization and amplitude estimation — important for clear-aligner, restorative, and occlusal models, where local deviations affect fit even with acceptable overall error.

3.8. Robustness Simulation under Scanning and Registration Noise

Robustness simulations at noise levels 0–50 μm (Figure 7) show all algorithms degrading, but HFBMM has the smallest slope: at 50 μm noise its RMSE is 0.064 mm versus 0.124 mm (linear regression) and 0.116 mm (Gaussian mixture regression).

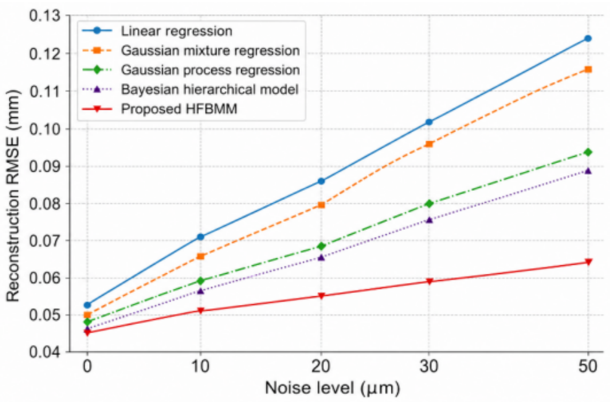

Fig. 7. Robustness comparison across algorithms under scanning and registration noise

This robustness comes from the Student-t likelihood limiting outlier influence, hierarchical random effects separating instance differences from residual noise, and fuzzy membership avoiding rigid boundary categories.

3.9. Posterior Uncertainty Decomposition

Figure 8's variance decomposition attributes 23% to build angle, 19% to local curvature, 16% to layer thickness, 12% to post-curing time, 11% to scanning noise, 10% to resin type, and 9% to individual model differences — build angle and local geometry dominate.

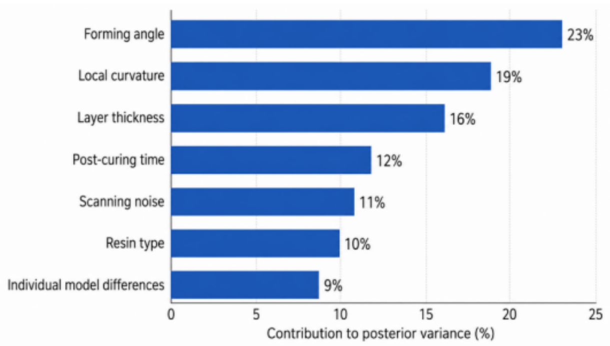

Fig. 8. Posterior uncertainty decomposition for printing and geometric factors

Practically, scanning-noise-driven uncertainty calls for better measurement/registration; build-angle/curvature-driven uncertainty calls for optimized orientation, slicing, and support design — turning decomposition into manufacturing guidance.

3.10. Tolerance-Exceedance Risk Map and Parameter Recommendations

Figure 9 shows the posterior probability map at $\tau = 0.10$ for local deviations exceeding the tolerance threshold. High-risk areas are mainly concentrated in cusps, marginal bevels, and support-adjacent areas of posterior teeth, whereas the smooth basal area is mostly low risk. The risk map is not identical to the original deviation field because it accounts for both the predicted mean and posterior variance. Some points may not have extreme predicted means, but because their posterior variance is large, their probability of exceeding the tolerance threshold may still be high.

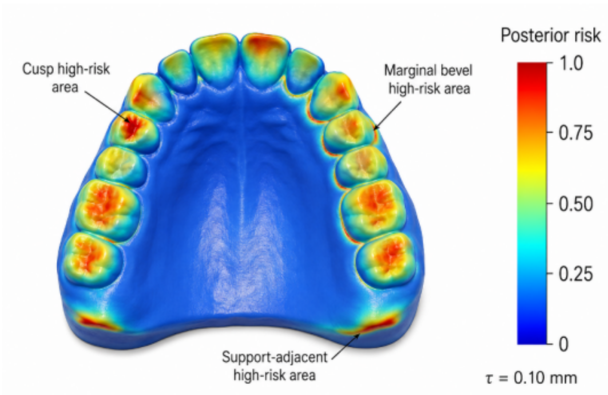

Fig. 9. Posterior tolerance-exceedance risk map for representative 3D-printed dental models

Table 6 shows that 50 μm/45° carries low predicted risk under SLA/DLP, while 100 μm/90° carries higher risk, especially under LCD (Category V). These labels denote benchmark-based process-risk categories derived from posterior simulation rather than clinical recommendations, and illustrate how posterior simulation can guide parameter selection rather than prescribe fixed clinical rules.

3.11. Number of Mixture Components and Threshold Sensitivity

Sensitivity analysis over K = 2–5 shows two components merge shrinkage and warping (reducing interpretability), three separate stable/deformation/noise but not shrinkage from expansion, four best balance WAIC and interpretability, and five lower training error but reduce label stability, so K = 4 was retained. Raising the tolerance threshold from 0.10 to 0.20 mm lowered model-level risk but left high-risk locations concentrated at cusps, margins, and

Table 6. Benchmark-Based Process-Risk Categories for Printing-Parameter Combinations

Printing technology	Layer thickness	Build angle	Predicted RMSE (mm)	Model-level risk $R_{\text{model}}(0.10)$	Benchmark risk category
DLP	50 μm	45°	0.034	0.061	Category I (lowest risk)
SLA	50 μm	45°	0.037	0.074	Category II (low risk)
DLP	100 μm	45°	0.049	0.138	Category III (moderate risk; inspection advised)
SLA	100 μm	90°	0.058	0.196	Category IV (elevated risk; conditional)
LCD	50 μm	45°	0.047	0.151	Category IV (elevated risk; conditional)
LCD	100 μm	90°	0.071	0.306	Category V (highest risk)

support-adjacent areas, showing the risk map reflects stable vulnerable regions rather than a threshold artifact.

3.12. Explanation of Key Findings

Deviations should be modeled as a 3D spatial random field, not a single aggregate error. HFBMM outperforms baselines by jointly capturing spatial heterogeneity, boundary ambiguity, and posterior uncertainty, reconstructing peaks, valleys, and steep transitions more accurately than linear regression, mixture-only modeling, Gaussian process regression, and Bayesian hierarchical modeling (Figs. 5–6). Rather than replacing experimental studies, HFBMM adds where errors occur, their likely mechanism, and their uncertainty — evidence suited to spatial quality control.

3.13. Relationship with Existing Dental 3D-Printing Research

This study complements prior work demonstrating multifactor dependence of dental-model accuracy on resin, printing technology, orientation, layer thickness, stacking, and storage [1–12]; rather than favoring a particular device or parameter, it proposes a probabilistic model spanning multiple factors, regions, and mechanisms — extending prior orientation/thickness findings into spatial posterior risk maps, color-deviation maps into computable posterior probability fields, and technology comparisons into cross-algorithm comparisons on the same deviation field.

3.14. Advantages of the Hybrid Fuzzy Bayesian Model

HFBMM's advantages operate at three levels: distributionally, the Student-t mixture likelihood handles non-normal, multimodal, long-tailed deviations without the outlier-skew risk of a Gaussian model; at the state-representation level, fuzzy membership captures continuous transitions among error states rarely caused by one mechanism; and at the decision level, the Bayesian posterior gives interval estimates and tolerance-exceedance probabilities more useful than point prediction alone. It is thus both predictive and explanatory, offering stronger interpretability than Gaussian process models and better handling of mixed mechanisms than conventional hierarchical or mixture-regression baselines, with the underlying paradigm extending to other free-form 3D-printed components (denture bases, surgical guides, implants, molds) sharing similar process-state ambiguity. These advantages are demonstrated here at the methodological level on the simulation benchmark; confirming them under physical manufacturing conditions is future work.

3.15. Engineering Application Significance

The following engineering-stage uses illustrate HFBMM's methodological potential within the present benchmark; clinical or manufacturing deployment requires further physical-data validation (see Future Research Directions). The model supports three engineering stages: pre-printing parameter screening (simulating risk maps across layer thickness, build angle, and post-curing time to select low-risk settings); post-printing quality inspection (using the scanned deviation field to identify whether shrinkage, support strategy, or registration is the likely cause); and process knowledge accumulation as posterior distributions update continuously. Unlike RMSE-threshold inspection, the posterior risk map divides the surface into low-, medium-, and high-risk areas, focusing inspection on cusps, thin margins, and support-adjacent regions.

3.16. Reproducibility: Simulation Data-Generating Process and Computational Details

To support reproducibility and reduce the risk of circular validation, the ground-truth deviation field was generated independently of the HFBMM likelihood (Eq. 11), using a physically motivated additive process rather than direct draws from a Student-t mixture. For printing instance i and surface point j, the simulated ground truth is defined as

$$e_{ij} = f_{\text{base}}(x_i, g_{ij}) + s_{ij} + w_{ij} + n_{ij} + \eta_i + \xi_{ij} \quad (20)$$

where f_base is a deterministic generalized-additive response surface in layer thickness, build angle, post-curing time, curvature, and support proximity, calibrated to the posterior effects in Table 3; s_ij, w_ij, and n_ij are independently sampled shrinkage, warping, and registration-noise terms; η_i is a model-level random offset; and ξ_ij is a spatially correlated Gaussian-process residual defined on the mesh graph. Table 7 lists the distribution and parameters used for each term.

Three features limit circularity between the generator and HFBMM: sij, wij, and nij are drawn independently per point from fixed marginal distributions with no mechanism label retained for training; f_base is a deterministic additive surface and ξij follows a Gaussian-process kernel, whereas HFBMM's mean structure and mixture weights (Eqs. 9–10) are estimated entirely from covariates, fuzzy memberships, and observed deviations, without access to the generator's functional form; and HFBMM's four latent components are not constrained to align one-to-one with the generator's four terms, with their weights, σk, and νk all inferred rather than specified. HFBMM therefore does not simply recover the generating equation; nevertheless, some structural favorability toward mixture-based models cannot be fully excluded, which is why physical, multi-device validation is prioritized in Future Research Directions. Because the benchmark contains approximately 14.4 million surface-point observations, exact Gaussian process regression is computationally infeasible. The GP baseline therefore uses a sparse variational approximation with 1,500 inducing points; Gaussian mixture regression and the Bayesian hierarchical model are fitted on a curvature- and region-balanced stratified 20% subsample ($\simeq$12.3M pts), selected after confirming that performance had stabilized beyond this size; HFBMM and linear regression use the full training set ($\simeq$11.5M pts). On common hardware (single NVIDIA A100 GPU, 256 GB RAM), training time / peak memory / inference throughput were: linear regression, 4 min / 3 GB / 2.1M pts/s; Gaussian mixture regression, 38 min / 12 GB / 310K pts/s; sparse Gaussian process regression, 3.1 h / 26 GB / 95K pts/s; Bayesian hierarchical model, 2.4 h / 19 GB / 140K pts/s; and HFBMM (NUTS, 4 chains), 6.8 h / 34 GB / 180K pts/s.

3.17. Limitations

First, this study focuses on dimensional deviations and does not jointly model surface roughness, material strength, long-term stability, cleaning residue, or biocompatibility. Second, fuzzy membership centers and widths still require preliminary experiments or expert settings rather than being learned within the Bayesian framework itself. Third, local neighborhood terms express spatial continuity without a full spatial random field or graph neural network, trading some representational capacity for interpretability and speed. Fourth, the 0.10 mm tolerance threshold is application-dependent and mainly for simulation; it should be adjusted for orthodontic, restorative, or diagnostic use. The reported numerical values should therefore be interpreted as benchmark evidence rather than direct clinical accuracy claims.

3.18. Future Research Directions

Priority extensions include validating HFBMM on real multi-device, multi-material, multi-scanner datasets by comparing STL deviation maps against this benchmark; embedding HFBMM in a Bayesian optimization loop where posterior risk maps guide active-learning parameter experiments; incorporating slicing paths, exposure energy, maintenance records, and post-curing logs into a real-time digital-twin posterior model; and exploring mesh graph neural networks and Gaussian Markov random fields, provided interpretability is maintained.

4. Conclusions

This study proposes a hybrid fuzzy Bayesian model for deviation analysis of 3D-printed dental models, representing each printed model as a three-dimensional signed deviation field that links local errors to printing parameters, geometric descriptors, and fuzzy memberships of error states. A Student-t mixture likelihood identifies latent deviation mechanisms, and Bayesian posterior inference quantifies prediction uncertainty and tolerance-exceedance risk. The simulation results show that the proposed model provides substantially greater information depth than conventional descriptive accuracy analysis: it reconstructs 3D dental-model surface deviations, identifies stable low-error, shrinkage, warping, and measurement-noise modes, and achieves lower prediction errors with better uncertainty calibration than the baseline algorithms, while maintaining strong robustness under scanning and registration noise and converting posterior predictions into interpretable risk maps and parameter recommendations. In particular, comparing 3D dental-model deviation fields across algorithms shows that uncertainty models for dental-model printing quality control must be evaluated at the three-dimensional surface level rather than relying solely on global RMSE. As the benchmark is simulation-driven, these findings should

Table 7. Distributions and Parameters Used to Generate the Simulation Benchmark

Component	Generative form	Key parameters
$f_{\text{base}}(x_i, g_{ij})$	Deterministic GAM response surface, calibrated to Table 3	e.g., 0.018 mm/100 μm layer thickness
Shrinkage s_{ij} / warping w_{ij}	Shifted Gamma (shape 2.2) / support-weighted Beta$(2, 5)$, mm	-0.02 to -0.06 mm / 0.03–0.07 mm
Noise n_{ij}	Student-t ($\nu = 4$), technology-dependent scale	0.008–0.015 mm
Random effect η_i / spatial residual ξ_{ij}	$\mathcal{N}(0, \tau^2)$ / Gaussian process, exponential kernel	$\tau = 0.006$ mm; SD 0.010 mm, length 2–8 mm

be read primarily as methodological validation of HFBMM; direct clinical or manufacturing applicability requires future validation on physical, multi-device data.

Acknowledgments

This work is supported by the Natural Science Foundation of Heilongjiang Province project: Engineering probiotics quantum dot composite system for temporal treatment of infectious bone defects (No. PL2025H010).

References

[1] E. S. Bud, V.-I. Bocanet, M. H. Muntean, A. Vlasa, S. M. Bucur, M. Păcurar, B. R. Dragomir, C. D. Olteanu, and A. Bud, (2021) *"Accuracy of Three-Dimensional (3D) Printed Dental Digital Models Generated with Three Types of Resin Polymers by Extra-Oral Optical Scanning"* **Journal of Clinical Medicine** ***10***(9): 1908. DOI: 10.3390/jcm10091908.

[2] F. Emir, G. Ceylan, and S. Ayyildiz, (2021) *"In Vitro Accuracies of 3D Printed Models Manufactured by Two Different Printing Technologies"* **European Oral Research** ***55***(2): 80–85. DOI: 10.26650/eor.20210060.

[3] J.-M. Park, J. Jeon, J.-Y. Koak, S.-K. Kim, and S.-J. Heo, (2021) *"Dimensional Accuracy and Surface Characteristics of 3D-Printed Dental Casts"* **The Journal of Prosthetic Dentistry** ***126***(3): 427–437. DOI: 10.1016/j.prosdent.2020.07.008.

[4] J. Ko, R. D. Bloomstein, D. Briss, J. N. Holland, H. M. Morsy, F. K. Kasper, and W. Huang, (2021) *"Effect of Build Angle and Layer Height on the Accuracy of 3-Dimensional Printed Dental Models"* **American Journal of Orthodontics and Dentofacial Orthopedics** ***160***(3): 451–458.e2. DOI: 10.1016/j.ajodo.2020.11.039.

[5] O. Hartley, T. Shanbhag, D. Smith, A. Grimm, Z. Salameh, S. K. Tadakamadla, F. Alifui-Segbaya, and K. E. Ahmed, (2022) *"The Effect of Stacking on the Accuracy of 3D-Printed Full-Arch Dental Models"* **Polymers** ***14***(24): 5465. DOI: 10.3390/polym14245465.

[6] M. Revilla-León, R. Cascos-Sánchez, J. M. Zeitler, A. B. Barmak, J. C. Kois, and M. Gómez-Polo, (2024) *"Influence of Print Orientation and Wet-Dry Storage Time on the Intaglio Accuracy of Additively Manufactured Occlusal Devices"* **The Journal of Prosthetic Dentistry** ***131***(6): 1226–1234. DOI: 10.1016/j.prosdent.2022.12.005.

[7] J.-H. Kim, J.-W. Choi, J.-J. Ahn, K.-B. Son, and J.-B. Huh, (2022) *"Accuracy Comparison among 3D-Printing Technologies to Produce Dental Models"* **Applied Sciences** ***12***(17): 8425. DOI: 10.3390/app12178425.

[8] A. Németh, V. Vitai, M. L. Czumbel, B. Szabó, G. Varga, B. Kerémi, P. Hegyi, P. Hermann, and J. Borbély, (2023) *"Clear Guidance to Select the Most Accurate Technologies for 3D Printing Dental Models: A Network Meta-Analysis"* **Journal of Dentistry** ***134***: 104532. DOI: 10.1016/j.jdent.2023.104532.

[9] V. Grassia, V. Ronsivalle, G. Isola, L. Nucci, R. Leonardi, and A. Lo Giudice, (2023) *"Accuracy (Trueness and Precision) of 3D Printed Orthodontic Models Finalized to Clear Aligners Production, Testing Crowded and Spaced Dentition"* **BMC Oral Health** ***23***: 352. DOI: 10.1186/s12903-023-03025-8.

[10] T. ElShebiny, S. Matthaios, L. M. Menezes, I. A. Tsolakis, and J. M. Palomo, (2024) *"Effect of Printing Technology, Layer Height, and Orientation on Assessment of 3D-Printed Models"* **Journal of the World Federation of Orthodontists** ***13***(4): 169–174. DOI: 10.1016/j.ejwf.2024.03.006.

[11] A. Wen, N. Xiao, Y. Zhu, Z. Gao, Q. Qin, S. Shan, W. Li, Y. Sun, Y. Wang, and Y. Zhao, (2024) *"Spatial Trueness Evaluation of 3D-Printed Dental Model Made of Photopolymer Resin: Use of Special Structurized Dental Model"* **Polymers *16***(8): 1083. DOI: 10.3390/polym16081083.

[12] M. A. Alghauli, S. A. Almuzaini, R. Aljohani, and A. Y. Alqutaibi, (2024) *"Impact of 3D Printing Orientation on Accuracy, Properties, Cost, and Time Efficiency of Additively Manufactured Dental Models: A Systematic Review"* **BMC Oral Health *24***: 1550. DOI: 10.1186/s12903-024-05365-5.

[13] N. Decker, M. Lyu, Y. Wang, and Q. Huang, (2021) *"Geometric Accuracy Prediction and Improvement for Additive Manufacturing Using Triangular Mesh Shape Data"* **Journal of Manufacturing Science and Engineering *143***(6): 061006. DOI: 10.1115/1.4049089.

[14] S. Goguelin, V. Dhokia, and J. M. Flynn, (2021) *"Bayesian Optimisation of Part Orientation in Additive Manufacturing"* **International Journal of Computer Integrated Manufacturing *34***(12): 1263–1284. DOI: 10.1080/0951192X.2021.1972466.

[15] S. Mahadevan, P. Nath, and Z. Hu, (2022) *"Uncertainty Quantification for Additive Manufacturing Process Improvement: Recent Advances"* **ASCE-ASME Journal of Risk and Uncertainty in Engineering Systems, Part B: Mechanical Engineering *8***(1): 010801. DOI: 10.1115/1.4053184.